Inorganic Chemistry

Article

pubs.acs.org/IC

Controlled Generation of Uniform Spherical $LaMnO_3$, $LaCoO_3$, Mn_2O_3, and Co_3O_4 Nanoparticles and Their High Catalytic Performance for Carbon Monoxide and Toluene Oxidation

Yuxi Liu, Hongxing Dai,* Jiguang Deng, Lei Zhang, Zhenxuan Zhao, Xinwei Li, Yuan Wang, Shaohua Xie, Huanggen Yang, and Guangsheng Guo

Laboratory of Catalysis Chemistry and Nanoscience, Department of Chemistry and Chemical Engineering, College of Environmental and Energy Engineering, Beijing University of Technology, Beijing 100124, P. R. China

Supporting Information

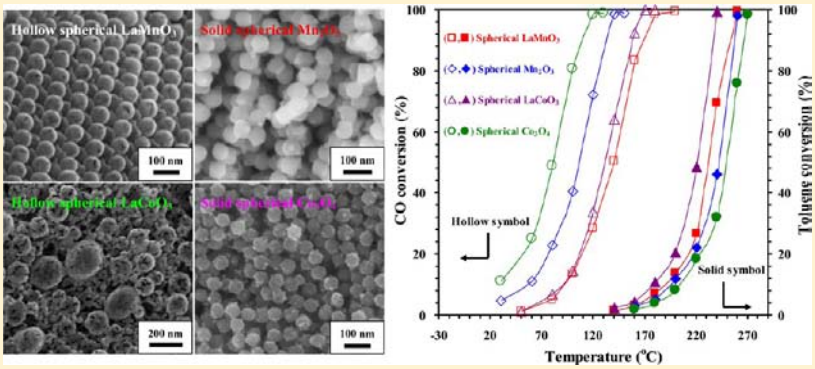

ABSTRACT: Uniform hollow spherical rhombohedral $LaMO_3$ and solid spherical cubic MO_x (M = Mn and Co) NPs were fabricated using the PMMA-templating strategy. Hollow spherical $LaMO_3$ and solid spherical MO_x NPs possessed surface areas of 21−33 and 21−24 m^2/g, respectively. There were larger amounts of surface-adsorbed oxygen species and better low-temperature reducibility on/of the hollow spherical $LaMO_3$ samples than on/of the solid spherical MO_x samples. Hollow spherical $LaMO_3$ and solid spherical MO_x samples outperformed their nanosized counterparts for oxidation of CO and toluene, with the best catalytic activity being achieved over the solid spherical Co_3O_4 sample for CO oxidation ($T_{50\%}$ = 81 °C and $T_{90\%}$ = 109 °C) at space velocity = 10 000 mL/(g h) and the hollow spherical $LaCoO_3$ sample for toluene oxidation ($T_{50\%}$ = 220 °C and $T_{90\%}$ = 237 °C) at space velocity = 20 000 mL/(g h). It is concluded that the higher surface areas and oxygen adspecies concentrations and better low-temperature reducibility are responsible for the excellent catalytic performance of the hollow spherical $LaCoO_3$ and solid spherical Co_3O_4 NPs. We believe that the PMMA-templating strategy provides an effective route to prepare uniform perovskite-type oxide and transition-metal oxide NPs.

INTRODUCTION

Hollow micro- and nanostructures have received much attention due to their potential applications as catalysts,[1] chemical sensors,[2] photonic devices,[3] chemical reactors,[4] and drug delivery.[5] Over the past decades, many efforts have been made in the development of different methods (e.g., template-free methods[6,7] and templating methods using either hard or soft templates[8,9]) for fabrication of hollow micro- and nanospheres. For example, Li et al. synthesized perovskite $LnFeO_3$ (Ln = La, Pr−Tb) hollow microspheres with a porous shell via a hydrothermal method.[10] Pan and co-workers prepared nearly monodispersed core−shell and hollow spherical $BaTiO_3$ nanoparticles through a one-pot template-free route in molten hydrated salt medium.[11] Lu et al. fabricated $BaZrO_3$ spheres using a facile modified hydrothermal approach in the presence of ethanol.[12] By hydrothermally treating the mixed solution of glucose, Fe^{3+}, and M^{2+} and after a calcination process, Gu et al. prepared MFe_2O_4 (M = Mg, Co, Ni, Zn) hollow spheres.[13] With porous carbon replica as the hard template, Kim et al. prepared $La_{0.7}Ca_{0.3}MnO_3$ hollow spheres.[14] Zhang et al. generated hollow spherical $LaMnO_3$ nanoparticles using the carbon spheres as the hard template.[15]

Metal oxide nanoparticles (NPs) usually possess high specific surface areas, facilitating interfacial processes when the NPs are used as catalyst. Generally speaking, there are two approaches to synthesize NPs: The "top-down" approach that utilizes physical methods and the "bottom-up" approach that employs solution-phase colloidal chemistry.[16] Recently, Stein and co-workers proposed a "disassembly strategy" for fabrication of metal oxide NPs, which involves the first inverse replication of colloidal crystals into a three-dimensionally ordered macro-

Received: April 4, 2013
Published: July 12, 2013

   dx.doi.org/10.1021/ic400832h | Inorg. Chem. 2013, 52, 8665−8676

Table 1. Preparation Parameters of the Spherical $LaMO_3$ and MO_x (M = Mn and Co) Samples

sample	metal source	total metal concentration (mol/L)	.solvent volumetric ratio (mL/mL/mL/mL)	.calcination condition
hollow spherical $LaMnO_3$	$La(NO_3)_3{\cdot}6H_2O$, $Mn(NO_3)_2$	1.0	PEG400/EG/MeOH = 5:3:10	300 °C 3 h (in N_2) → 750 °C 4 h (in air)
solid spherical Mn_2O_3	$Mn(NO_3)_2{\cdot}4H_2O$	1.5	PEG400/EG/MeOH/H_2O = 5:3:7:5	300 °C 3 h (in N_2) → 450 °C 4 h (in air)
hollow spherical $LaCoO_3$	$La(NO_3)_3{\cdot}6H_2O$, $Co(NO_3)_2{\cdot}6H_2O$	1.0	PEG400/EG/MeOH/H_2O = 7:3:7:5	300 °C 3 h (in N_2) → 650 °C 4 h (in air)
solid spherical Co_3O_4	$Co(NO_3)_2{\cdot}6H_2O$	1.5	PEG400/EG/MeOH/H_2O = 5:8:2:5	300 °C 3 h (in N_2) → 450 °C 4 h (in air)

porous (3DOM) structure and follows the disassembly process for generation of shaped building blocks.[17,18] Manganese oxide or cobalt oxide (MO_x, M = Mn and Co) and lanthanum manganite or cobaltite ($LaMO_3$, M = Mn and Co) have many applications in catalysis,[19,20] energy conversion,[21] and sensing.[19] It has been well established that the behaviors of nanoscale materials strongly depend on the shape and size of the particles, which are key factors influencing their ultimate performance. Hence, it is highly desired to develop an effective method for controlled preparation of $LaMO_3$ and MO_x with uniform morphologies so that their performance can be enhanced.

It has been generally accepted that supported noble metals, single transition-metal oxides, and mixed metal oxides (e.g., perovsike-type oxides) are active toward oxidation of CO and volatile organic compounds (VOCs). Although the supported noble metals exhibit excellent catalytic activity, the expensive cost and easily poisoned tendency limit their wide applications. The other two kinds of catalysts, however, have the advantages of cheapness and good catalytic activities. Manganese oxide and cobalt oxide have attracted much attention due to their promising catalytic properties. As oxidation catalysts, manganese oxide and cobalt oxide show good catalytic performance for removal of CO and VOCs.[22−24] For instance, Garcia et al. found that Co_3O_4 performed well in the deep oxidation of a series of representative VOCs.[25] Schüth and co-workers observed that the porous Co_3O_4 material was an excellent catalyst for oxidation of CO.[26] Bruce et al. claimed that mesoporous Co_3O_4, Cr_2O_3, Fe_2O_3, Mn_2O_3, and Mn_3O_4 showed good catalytic performance for CO oxidation.[27] Xie et al. reported that nanorod-like Co_3O_4 exhibited excellent catalytic activities for low-temperature oxidation of CO.[24] Our group found that mesoporous cobalt oxide and manganese oxide performed well in the combustion of toluene.[28,29] Among the perovsike-type oxide catalysts, the manganite and cobaltite ones perform best for complete oxidation of CO and VOCs.[19,27,30,31] For example, After examining the catalytic activity of $LaMnO_3$, Irusta et al. found that 90% toluene conversion was reached at ca. 290 °C and 178 h^{-1}.[30] Over the $LaMnO_3$ catalyst at ca. 335 °C and 14 000 h^{-1}, 90% benzene conversion could be obtained.[31]

Herein we report a facile and effective strategy for controlled fabrication of monodispersed spherical $LaMO_3$ and MO_x (M = Mn and Co) NPs, which uses the polymethyl methacrylate (PMMA) colloidal crystal as a hard template and the surfactant (poly(ethylene glycol) (PEG) or ethylene glycol (EG)) as a soft template. To the best of our knowledge, it is the first time to report the synthesis of uniform spherical $LaMO_3$ and MO_x NPs. This work provides an effective strategy for controlled generation of uniform spherical perovskite-type oxides and transition-metal oxides and their catalytic applications in CO and toluene oxidation.

EXPERIMENTAL SECTION

Catalyst Preparation. The well-arrayed colloid crystal template PMMA microspheres with an average diameter of ca. 300 nm (Figure S1, Supporting Information) were synthesized according to the procedures described elsewhere.[32] $LaMO_3$ and MO_x (M = Mn and Co) samples were prepared using the PEG-assisted PMMA-templating strategy. In a typical fabrication procedure, stoichiometric amounts of metal nitrates were dissolved in a mixed solution of PEG (MW = 400 g/mol), EG, water, and methanol (MeOH) at room temperature (RT) under stirring for 4 h to obtain a transparent solution (preparation parameters are summarized in Table 1). Then, the PMMA template was added to the transparent solution and soaked for 5 h. After being filtered, the mixture was dried at RT for 48 h; the obtained powders were subsequently heated in N_2 (200 mL/min) at 300 °C for 3 h, cooled to 50 °C in the same atmosphere, and finally calcined in air (250 mL/min) at a certain temperature (450−750 °C) for 4 h to remove the template, thus generating the spherical samples. For comparison purposes, the nanosized $LaMnO_3$ and $LaCoO_3$ samples were prepared via the Pechini method[33] and after calcination at 850 and 750 °C, respectively; the nanosized MO_x (i.e., Mn_2O_3 and Co_3O_4) samples were also prepared via the thermal decomposition method with $Mn(NO_3)_2{\cdot}4H_2O$ and $Co(NO_3)_2{\cdot}6H_2O$ as the metal source and after calcination at 700 °C for 5 h.

The chemicals (A.R. in purity) were purchased from Sinopharm Chemical Reagent Beijing Co. and used without further purification.

Catalyst Characterization. X-ray diffraction (XRD) patterns of the samples were recorded on a Bruker D8 Advance diffractometer with Cu Kα radiation and a nickel filter (λ = 0.15406 nm). BET (Brunauer−Emmett−Teller) surface areas of the samples were measured via N_2 adsorption at −196 °C on a Micromeritics ASAP 2020 analyzer with samples being outgassed at 250 °C for 3 h under vacuum before measurement. Scanning electron microscopic (SEM) images of the samples were recorded on a Gemini Zeiss Supra 55 apparatus (operating at 10 kV). Transmission electron microscopic (TEM) images of the samples were obtained using the JEOL-2010 equipment (operating at 200 kV). Thermogravimetric analysis (TGA) and differential scanning calorimetric (DSC) analysis of the samples were conducted on a SDT Q600 (TA) apparatus. Fourier transform infrared (FT-IR) spectra of the samples (1 wt % sample +99 wt % KBr) were obtained in the region of 400−4000 cm^{-1} with a resolution of 4 cm^{-1} on a Bruker Vertex 70 spectrometer. X-ray photoelectron spectroscopy (XPS, VG CLAM 4 MCD analyzer) was used to determine the La 3d, Mn 2p, Co 2p, O 1s, and C 1s binding energies (BEs) of surface species using Mg Kα ($h\nu$ = 1253.6 eV) as the excitation source. Before XPS measurement, the sample was pretreated in an O_2 flow of 20 mL/min at 500 °C for 1 h. After being cooled to RT, the pretreated sample was transferred to a holder in a glove bag (Instruments for Research and Industry) that was filled with helium, and then the holder was transferred into the spectrometer chamber under helium. Before being analyzed in the analysis chamber, the pretreated sample was outgassed in the preparation chamber for 0.5 h. The C 1s signal at BE = 284.6 eV was taken as a reference for BE calibration. XPS spectra of the samples were decomposed using the curve-fitting CasaXPS Program.

Hydrogen temperature-programmed reduction (H_2-TPR) experiments were carried out on a chemical adsorption analyzer (Autochem II 2920, Micromeritics). Before TPR measurement, ca. 0.02 g of

dx.doi.org/10.1021/ic400832h | Inorg. Chem. 2013, 52, 8665−8676

catalyst (40−60 mesh) was first treated in an oxygen flow of 30 mL/min at 500 °C for 1 h in a quartz fixed-bed U-shaped microreactor (i.d. = 4 mm). After being cooled at the same atmosphere to RT, the pretreated sample was exposed to a flow (50 mL/min) of 5% H_2−95% Ar (v/v) mixture and heated from RT to 850 °C at a ramp of 10 °C/min. The variation in H_2 concentration of the effluent was monitored online by the chemical adsorption analyzer. The reduction band was calibrated against that of the complete reduction of a known standard of powdered CuO (Aldrich, 99.995%).

Catalytic Evaluation. Catalytic activity was evaluated with the sample being charged in a continuous flow fixed-bed quartz microreactor (i.d. = 4 mm). To minimize the effect of hot spots, the sample (50 mg, 40−60 mesh) was diluted with 0.25 g of quartz sands (40−60 mesh). Prior to the test, all of the samples were treated in air (30 mL/min) at 400 °C for 0.5 h and then cooled to a given temperature. (i) In the case of CO oxidation, the CO-containing reactant gas (1 vol % CO + 20 vol % O_2 + N_2 (balance)) was passed through the sample bed; the space velocity (SV) was ca. 10 000 mL/(g h). Reactants and products were analyzed online by a gas chromatograph (GC-14C, Shimadzu) equipped with a thermal conductivity detector (TCD) using a 13X column. (ii) In the case of toluene oxidation, the total flow rate of the reactant mixture (1000 ppm toluene + O_2 + N_2 (balance)) was 33.3 mL/min, giving a toluene/O_2 molar ratio of 1/400 and a space velocity (SV) of 20 000 mL/(g h). The 1000 ppm toluene was generated by passing a N_2 flow through a bottle containing pure toluene (A.R. grade) chilled in an ice−water isothermal bath. Reactants and products were analyzed online by a gas chromatograph (GC-2010, Shimadzu) equipped with a flame ionization detector (FID) and a thermal conductivity detector (TCD) using a stabilwax@-DA column (30 m in length) for VOC separation and a 1/8 in Carboxen 1000 column (3 m in length) for permanent gas separation. Using a mass spectrometer (HPR20, Hiden), we only detected toluene, carbon dioxide, and water in the outlet gas mixture from the microreactor. The balance of carbon throughout the investigation was estimated to be 99.5%. Relative errors for the gas concentration measurements were less than ±1.5%.

RESULTS AND DISCUSSION

Crystal Structure and Surface Area. Figure 1 shows the XRD patterns of the spherical $LaMO_3$ and MO_x samples. By comparing the XRD patterns (Figure 1a and 1b) of the rhombohedral $LaMnO_3$ (JCPDS PDF 82-1152) and rhombohedral $LaCoO_3$ (JCPDS PDF 48-0123) samples, it can be realized that the spherical $LaMnO_3$ and $LaCoO_3$ samples possessed a single-phase rhombohedral crystal structure, and their corresponding crystallite sizes were about 31.1 and 29.2 nm. From the XRD patterns (Figure 1c and 1d) of the solid spherical Mn_2O_3 (JCPDS PDF 41-1442) and Co_3O_4 (JCPDS PDF 43-1003) samples it can be deduced that the solid spherical Mn_2O_3 and Co_3O_4 samples were of single-phase cubic crystal structure. Nitrogen adsorption−desorption isotherms of the spherical $LaMO_3$ and MO_x samples are shown in Figure S2, Supporting Information. These isotherms could be categorized to type III with a type H3 hysteresis loop in the relative pressure (p/p_0) range of 0.8−1.0. The type H3 hysteresis loop is usually related to the existence of slit-shaped pores in materials, indicative of a pore size distribution extending to the macropore range. All of the samples possessed pore-size distributions scattered from 2 to 80 nm. From Table 2, it can be seen that the surface areas (ca. 21 m^2/g) of the spherical $LaCoO_3$ and Co_3O_4 samples were lower than those (24−33 m^2/g) of the spherical $LaMnO_3$ and Mn_2O_3 samples.

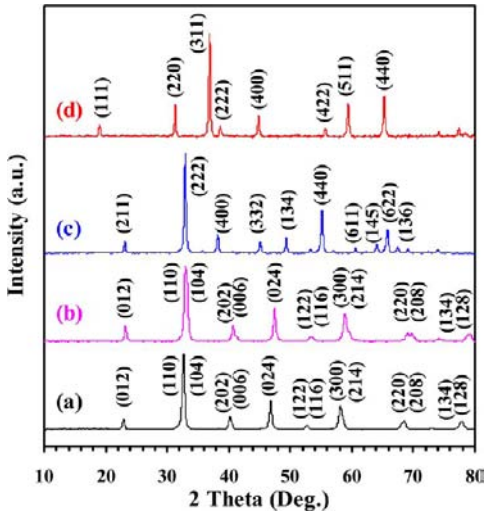

Figure 1. XRD patterns of (a) hollow spherical $LaMnO_3$, (b) hollow spherical $LaCoO_3$, (c) solid spherical Mn_2O_3, and (d) solid spherical Co_3O_4.

Morphology. Figure 2 shows the SEM images of the $LaMO_3$ and MO_x samples. The $LaMnO_3$ sample was uniform spherical in morphology (Figure 2a and 2b) and had a narrow size distribution in the range of 65−75 nm. Solid spherical Mn_2O_3 NPs were approximately 50 nm in diameter (Figure 2c and 2d). The $LaCoO_3$ sample contained hollow spherical $LaCoO_3$ NPs (Figure 2e and 2f), whereas the Co_3O_4 sample was composed of solid spherical Co_3O_4 NPs (Figure 2g and 2h). Figure 3 shows the typical TEM images and SAED patterns of the $LaMO_3$ and MO_x samples. The shell of the hollow spherical $LaMnO_3$ NPs was about 12 nm in thickness. From the high-resolution TEM (HRTEM) image (Figure 3b) of the hollow spherical $LaMnO_3$ NPs, the intraplanar spacing was measured to be 0.280 nm, in good agreement with that of the (110) crystal plane of the standard $LaMnO_3$ sample (JCPDS PDF 82-1152). The HRTEM image (Figure 3d) also gives evidence that the solid spherical Mn_2O_3 NPs were highly crystalline, and the lattice spacing of 0.270 nm could be indexed to the (222) plane of the standard Mn_2O_3 sample (JCPDS PDF 41-1442). Observation of multiple bright electron diffraction rings in the inset SAED patterns of the spherical $LaMnO_3$ and Mn_2O_3 samples suggests formation of polycrystalline structure. From the HRTEM image (Figure 3f) of the hollow spherical $LaCoO_3$ NPs, the lattice spacing was ca. 0.270 nm, in good agreement with that of the (110) crystal plane of the standard $LaCoO_3$ sample (JCPDS PDF 48-0123). The solid spherical Co_3O_4 sample was composed by a number of aggregated NPs (Figure 3g). The HRTEM image (Figure 3h) suggests that the solid spherical Co_3O_4 NPs were highly crystalline, and lattice spacings of 0.290 and 0.140 nm could be indexed to the (220) and (440) planes of the standard Co_3O_4 sample (JCPDS PDF 43-1003), respectively. Recording of multiple bright electron diffraction rings in the inset SAED patterns (insets of Figure 3f and 3h) of the spherical $LaCoO_3$ and Co_3O_4 samples was indicative of formation of polycrystalline structure.

Formation Mechanism. Figure 4A shows the TGA/DSC profiles of the hollow spherical $LaMnO_3$ precursor under a flowing N_2 atmosphere. The first weight loss (ca. 10.9 wt %) was observed in the range of RT−253 °C due to formation of metal−PEG (EG) complexes and NO_x via reaction of PEG (EG) with the metal nitrates[34,35] and decomposition of EG,[35] accompanying the appearance of endothermic signals centered at 119, 171, and 229 °C; the second weight loss (ca. 12.2 wt %) appeared in the range of 253−295 °C due to decomposition of the remaining PEG (boiling point =250 °C), accompanying the

dx.doi.org/10.1021/ic400832h | Inorg. Chem. 2013, 52, 8665−8676

Table 2. Crystallite Sizes (D), BET Surface Areas, and Surface Element Compositions of the Spherical $LaMO_3$ and MO_x (M = Mn and Co) Samples

sample	particle dimension[a] (nm)	D[b] (nm)	surface area (m^2/g)	surface La/Mn or La/Co molar ratio[c] (mol/mol)	surface Mn^{4+}/Mn^{3+} or Co^{3+}/Co^{2+} molar ratio (mol/mol)	surface O_{ads}/O_{latt} molar ratio (mol/mol)
hollow spherical $LaMnO_3$	70	31.1	32.5	1.19 (1.00)	1.05	0.89
solid spherical Mn_2O_3	50	43.4	24.0		2.09[d]	0.76
hollow spherical $LaCoO_3$	90−200	29.2	20.7	1.43 (1.00)	1.82	1.28
solid spherical Co_3O_4	55	54.0	20.9		0.83	0.92
used hollow spherical $LaCoO_3$[e]					1.96	1.06
used solid spherical Co_3O_4[f]					0.92	0.84

[a]Estimated according to the SEM and TEM images. [b]Data determined according to the Scherrer equation using the fwhm of the (110) lines of $LaMnO_3$ and $LaCoO_3$, the (222) line of Mn_2O_3, and the (311) line of Co_3O_4. [c]Data in parentheses are estimated according to the nominal bulk compositions. [d]Data in parentheses is the surface Mn^{3+}/Mn^{2+} molar ratio. [e]Hollow spherical $LaCoO_3$ sample after 100 h of on-stream reaction for toluene oxidation under the conditions of toluene concentration = 1000 ppm, toluene/O_2 molar ratio = 1/400, SV = 20 000 mL/(g h), and temperature = 230 °C; [f]Solid spherical Co_3O_4 sample after 100 h of on-stream reaction for CO oxidation under the conditions of CO concentration = 1 vol %, CO/O_2 molar ratio = 1/20, SV = 10 000 mL/(g h), and temperature = 100 °C.

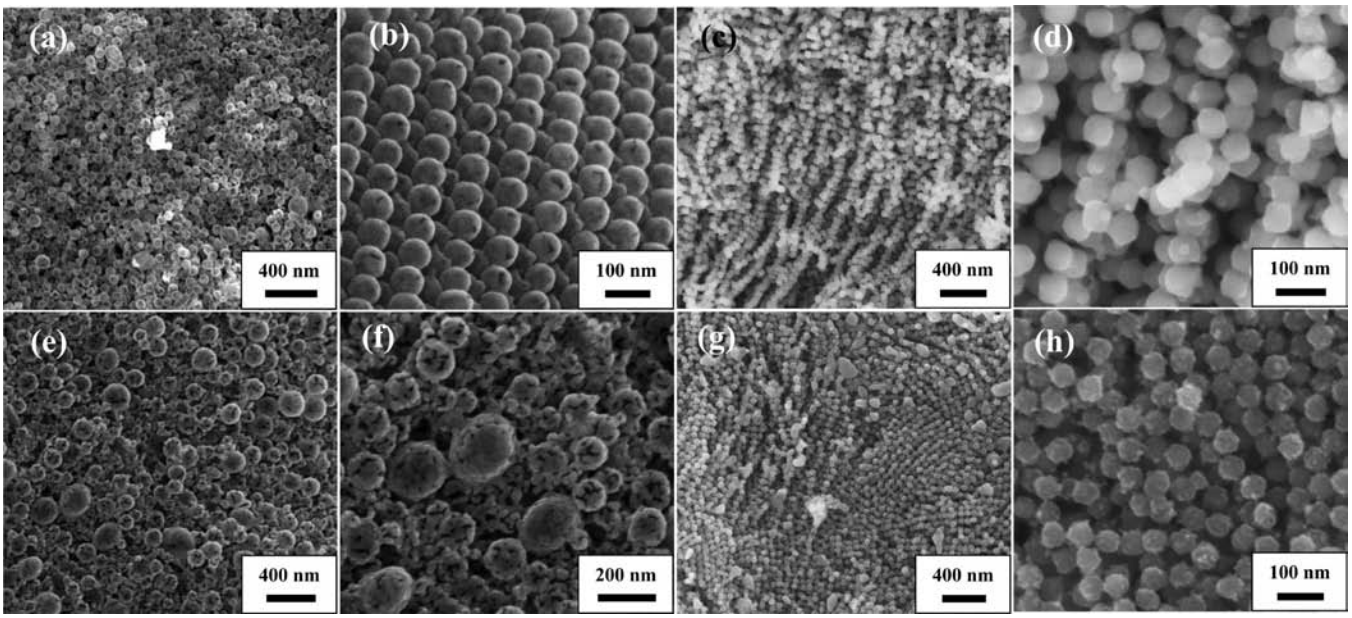

Figure 2. SEM images of (a, b) hollow spherical $LaMnO_3$, (c, d) solid spherical Mn_2O_3, (e, f) hollow spherical $LaCoO_3$, and (g, h) solid spherical Co_3O_4.

recording of an endothermic signal at 274 °C; the third weight loss (ca. 67.3 wt %) in the 295−493 °C range was attributable to decomposition of the metal−PEG (EG) complexes and partial decomposition of PMMA,[34,36] together with detection of an endothermic signal at 380 °C. After being calcined in N_2 at 300 °C, the partially carbonized intermediate product was further investigated by TGA/DSC in air (Figure 4B). There was one small weight loss (ca. 2.6 wt %) below 264 °C and one big weight loss (ca. 85.8 wt %) in the range of 264−450 °C, in the meanwhile endothermic signals centered at 310 and 378 °C were detected. The former weight loss was due to the removal of adsorbed water, whereas the latter weight loss was reasonably assigned to the elimination of the partially carbonized PMMA and the oxidative decomposition of the metal−PEG (EG) complexes to oxycarbonate.[34,36] Therefore, we conclude that most of the PMMA was partially carbonized after calcination in N_2 at 300 °C, which could act as a template for generation of mixed metal oxide nanostructured framework.

The XRD patterns of the products obtained at different preparation steps are shown in Figure 5. The single-phase and well-crystallized perovskite phase was detected after thermal treatment in air at 750 °C. The hollow spherical $LaMnO_3$ precursor treated in N_2 at 300 °C showed several wide peaks characteristics of an amorphous metal−organic complex phase. After being calcined in air at 350 °C, these peaks disappeared. When the treatment temperature rose to 500 or 650 °C in air, the XRD pattern showed a weak and wide peak at 2θ = 30.4°, which could be assigned to the lanthanum oxycarbonate $La_2O_2(CO_3)$ phase (JCPDS PDF 84-1963).

FT-IR spectra of the samples are shown in Figure 6. The spectrum (Figure 6a) of the precursor dried at RT displayed numerous absorption bands. The absorption band at ca. 568

dx.doi.org/10.1021/ic400832h | Inorg. Chem. 2013, 52, 8665−8676

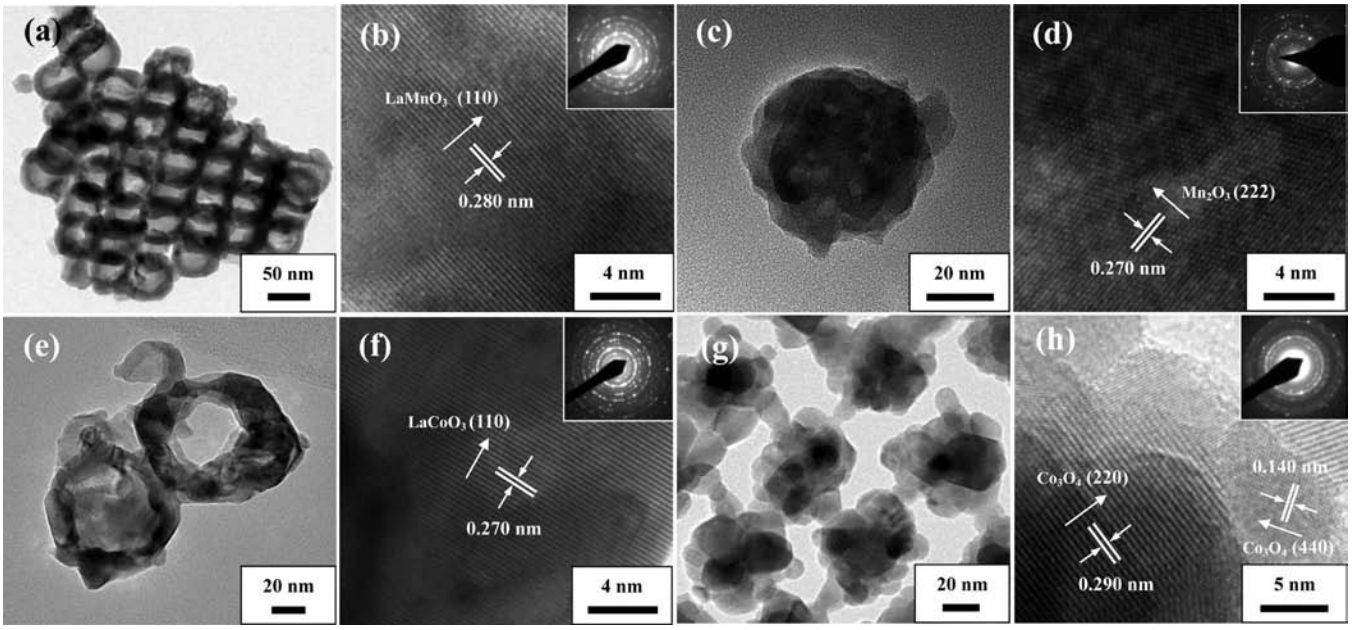

Figure 3. TEM images and SAED patterns (insets) of (a, b) hollow spherical $LaMnO_3$, (c, d) solid spherical Mn_2O_3, (e, f) hollow spherical $LaCoO_3$, and (g, h) solid spherical Co_3O_4.

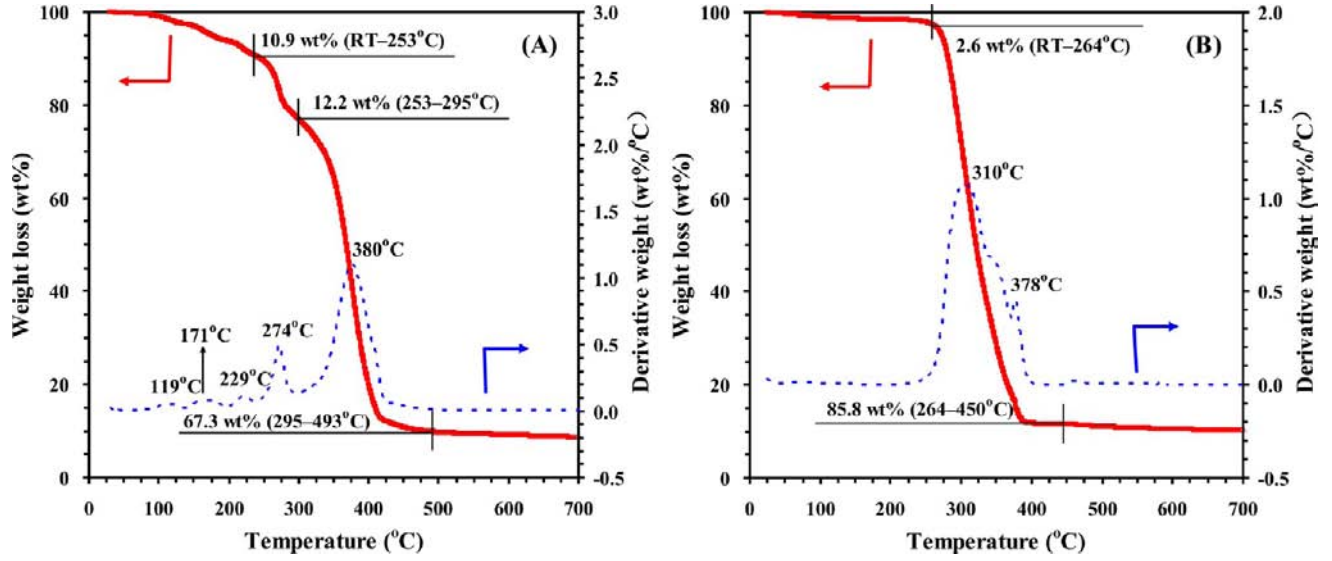

Figure 4. TGA/DSC profiles of (A) the spherical $LaMnO_3$ precursor determined in a N_2 flow and (B) the 300 °C calcined in N_2 spherical $LaMnO_3$ precursor determined in an air flow.

cm^{-1} corresponded to the stretching mode of the M−O−M or M−O bond in metal nitrates.[37] An absorption band at 3410 cm^{-1} was due to the stretching vibrations of water.[38] Absorption bands at 2964 and 3010 cm^{-1} were assignable to the symmetric and asymmetric stretching vibrations of the CH_2 groups and the terminal CH_3 group in the PEG, EG, and PMMA.[39] Absorption bands at 1456 and 1741 cm^{-1} corresponded to the symmetric and asymmetric stretching vibrations of COO^-,[40,41] respectively. The absorption band at 1645 cm^{-1} was due to the stretching vibration of C═O bonds,[40] the ones at 1095, 1157, and 1199 cm^{-1} were due to the stretching vibrations of C−O (ester bonds),[38,42] and the ones at 755, 844, and 985 cm^{-1} were due to the bending vibrations of C−H bonds,[38] whereas the absorption band at 1380 cm^{-1} could be assigned to the N−O stretching vibration of nitrate.[43] After thermal treatment in N_2 at 300 °C, the intensity of the absorption bands decreased significantly but not completely disappeared, indicating that organic components such as partially carbonized PMMA were still retained under this condition, which is also confirmed by the TGA/DSC results (Figure 4). Spectra of the samples further calcined in air at 350, 500, and 650 °C (Figure 6c−e) showed a stronger reduction in water content, and absorption bands corresponding to the organic species disappeared. New broad absorption bands appeared at 1395, 1485, and 850 cm^{-1}, and their intensity decreased with increase rise in annealing temperature; these absorption bands could be attributed to the vibrations (ν_{as}(COO) and ν_s(COO)) of CO_3^{2-}.[44] Spectra of the samples pretreated in air at 350, 500, 650, and 750 °C also showed a strong absorption band at 621−642 cm^{-1} (Figure 6c−f), typical of the metal−oxygen bonds. Furthermore, the intensity of this band almost remained unchanged with the rise in annealing

dx.doi.org/10.1021/ic400832h | Inorg. Chem. 2013, 52, 8665−8676

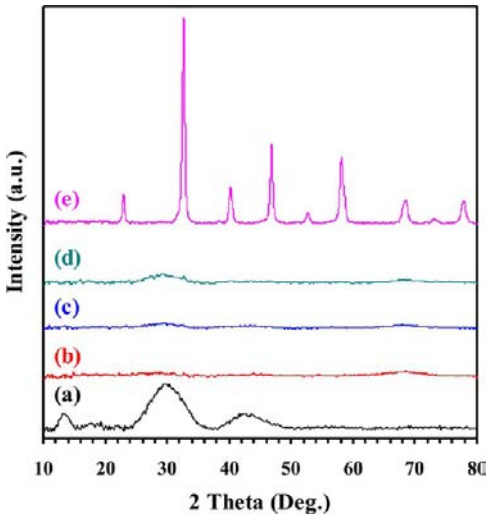

Figure 5. XRD patterns of the spherical $LaMnO_3$ precursors calcined in (a) N_2 at 300 °C, (b) air at 350 °C, (c) air at 500 °C, (d) air at 650 °C, and (e) air at 750 °C.

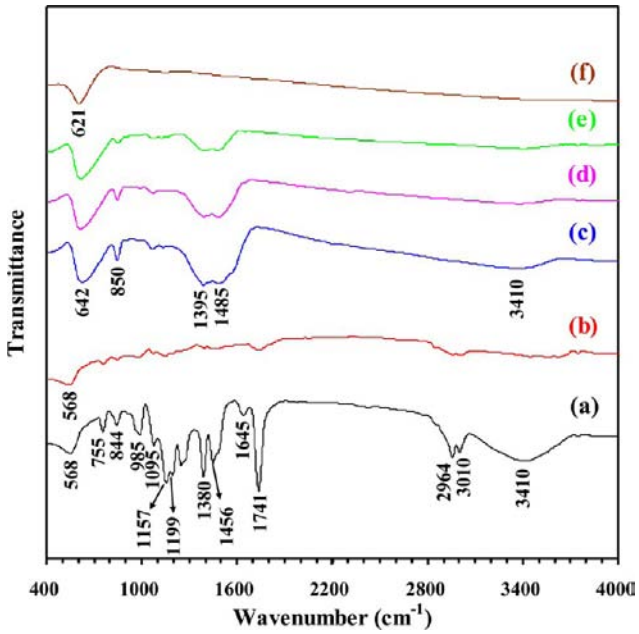

Figure 6. FT-IR spectra of the spherical $LaMnO_3$ precursors (a) before calcination and calcined (b) in N_2 at 300 °C, (c) in air at 350 °C, (d) in air at 500 °C, (e) in air at 650 °C, and (f) in air at 750 °C.

temperature. According to the FT-IR spectrum of the uncalcined sample, it can be known that there were adsorbed H_2O and PEG (EG) on the uncalcined PMMA-containing sample, and the amounts of these adspecies decreased significantly after thermal treatment in N_2 atmosphere; after further calcination in air at 350 °C they disappeared, but a large amount of metal oxycarbonates was generated; these metal oxycarbonate species remained after calcination in air at 650 °C and finally disappeared after calcination in air at 750 °C. Therefore, FT-IR results indicate that lanthanum oxycarbonate was formed and needed a higher temperature to be decomposed.

Figure 7 shows the SEM and TEM images of the hollow spherical $LaMnO_3$ precursors under different calcination conditions. Solid spherical $LaMnO_3$ precursor containing partially carbonized PMMA was obtained after calcination in N_2 at 300 °C (Figure 7a and 7b) or in air at 350 °C (Figure 7c and 7d). After calcination in air at 500 °C (Figure 7e and 7f) or in air at 650 °C (Figure 7g and 7h), however, hollow spherical $LaMnO_3$ precursor was generated due to removal of PMMA template.

It is interesting to understand the formation mechanism of the hollow spherical $LaMO_3$ and solid spherical MO_x NPs. There are two main mechanisms for formation of spherical NPs. One is based on the Kirkendall effect,[45,46] which originates from the difference in the diffusion rate of two interdiffusion species across an interface. The net flow of mass in one direction is balanced by an opposite flux of vacancies, which may then coalesce into inner voids preferably around the interface. The other is the Ostwald ripening mechanism.[6,7,47] Because of the intrinsic density variation inside the starting solid particles, the inner space can be created when the less stable parts (smaller or loosely packed crystallites) in the particles undergo mass transport through dissolution and recrystallization. From the above results, we believe that the Ostwald ripening mechanism governs formation of spherical $LaMO_3$ and MO_x NPs in this study, and the formation process of hollow and solid spherical $LaMO_3$ and MO_x NPs is illustrated in Scheme 1. Usually a polymer template like PMMA or polystyrene can function as a support for conversion of metal precursor to a solid-state framework (e.g., metal glyoxylates) at a low temperature and gives rise to the 3DOM-structured pure or mixed metal oxides after removal of the polymer template.[48] The glass transition temperature of PMMA in air was ca. 130 °C.[49] The decomposition temperature of cobalt nitrate was close to the glass transition temperature of PMMA. With the glass transition of the PMMA, solidification due to decomposition of metal nitrate and complexing of metal nitrate with PEG (EG) would take place concurrently, and some of the metal salts are squeezed out from the voids of the polymer template, hence resulting in a low fraction and deformation of primary spherical structure.[50] Therefore, it is difficult to prepare high-quality uniform hollow spherical $LaCoO_3$ materials. For the pure cobalt oxide, however, the cobalt precursor concentration was high enough to maintain the particle morphology, even though some of the cobalt precursor was squeezed out from the template. As we know, PEG is generally used as a surfactant or chelating agent with high viscosity.[51,52] In the present investigation, a large amount of PEG (EG) and a low concentration of metal salt were used as the precursor solution, which was infiltrated into the voids of the PMMA template. During removal of the low boiling point solvent, the PEG (EG) could react with the metal ions to form the metal−PEG (EG) complexes. When the temperature rose further, the metal−PEG (EG) complexes covered the surfaces of the partially carbonized PMMA spheres to generate a shell of the metal−PEG (EG) complexes. After removal of the partially carbonized PMMA beads in air, the metal−PEG (EG) complexes decomposed oxidatively and contracted to form the hollow spherical $LaMO_3$ NPs through shrinking of the shell for minimization of total surface energy, thus obtaining the hollow spherical $LaMO_3$ NPs. As for formation of solid spherical MO_x NPs, we believe that without introduction of lanthanum oxidative decomposition of the M−PEG (EG) complexes is a quick process and the primarily formed manganese oxide or cobalt oxide nanocrystals grew up fast to generate the solid spherical MO_x NPs.

dx.doi.org/10.1021/ic400832h | Inorg. Chem. 2013, 52, 8665−8676

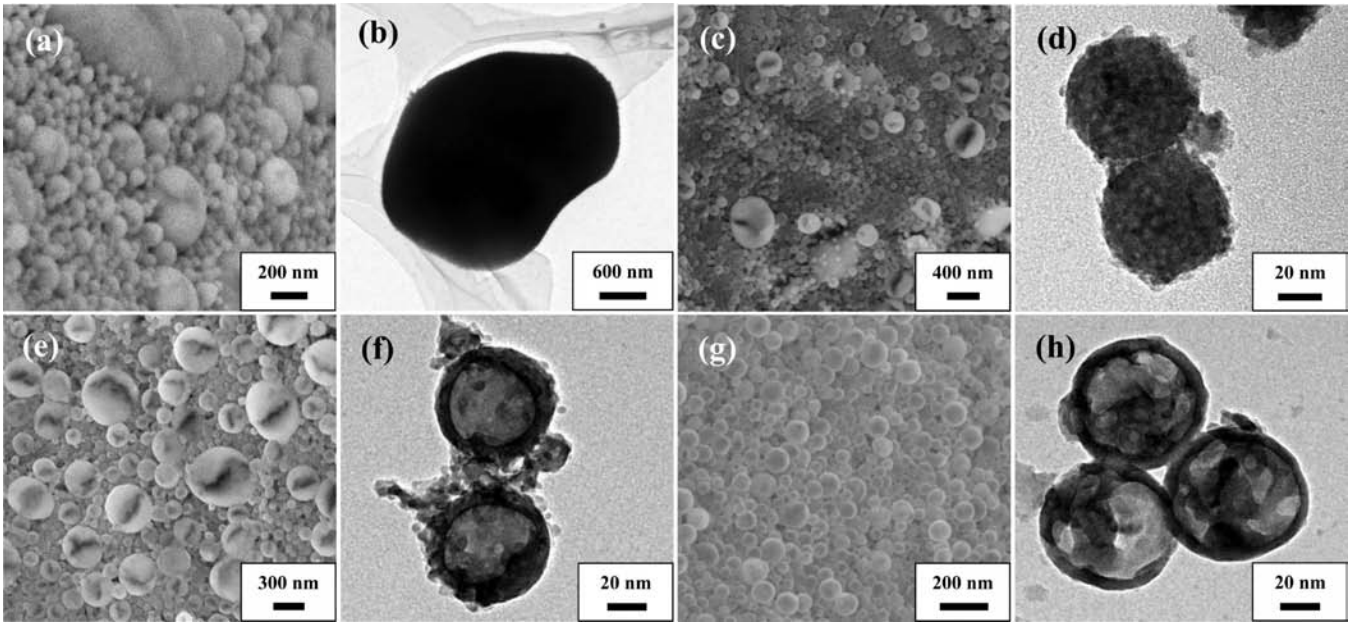

Figure 7. SEM and TEM images of the spherical $LaMnO_3$ precursors calcined in (a, b) N_2 at 300 °C, (c, d) air at 350 °C, (e, f) air at 500 °C, and (g, h) air at 650 °C.

Scheme 1. Schematic Illustration of the Formation Mechanism of the Hollow Spherical $LaMO_3$ and Solid Spherical MO_x Samples

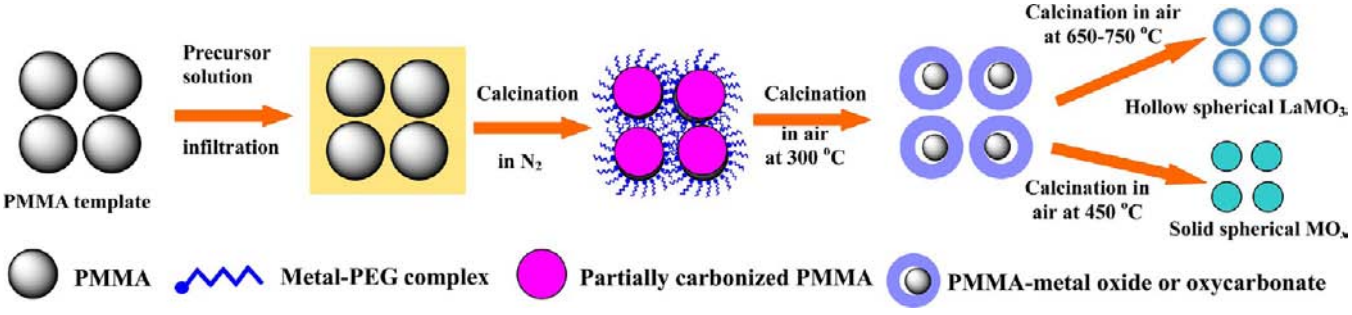

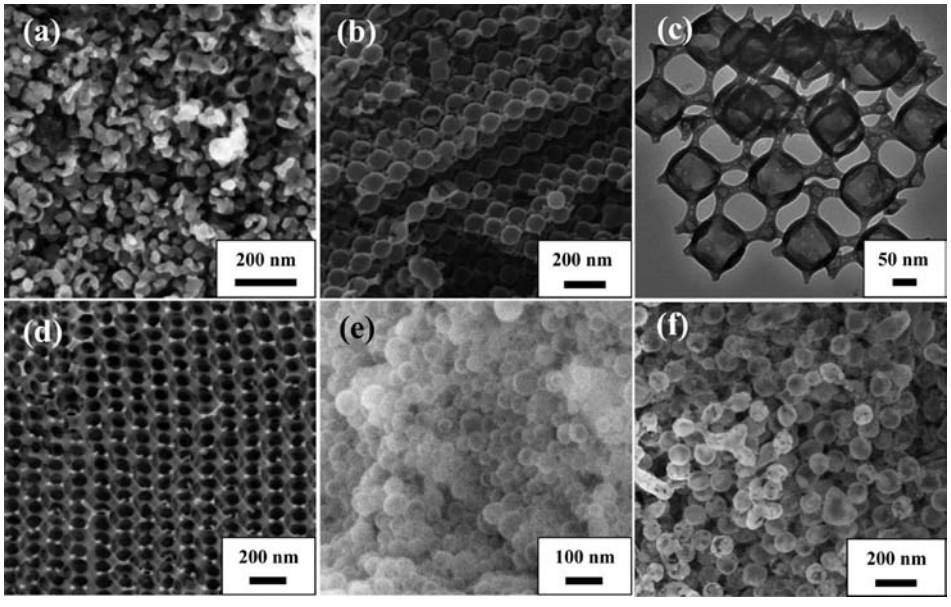

Figure 8. SEM and TEM images of the $LaMnO_3$ samples prepared at a total metal concentration of (a) 0.5 moL/L and (b, c) 2.5 moL/L, (d) in the absence of PEG, (e) at a PEG amount of 3 mL, and (f) at a PEG amount of 8 mL.

dx.doi.org/10.1021/ic400832h | *Inorg. Chem.* 2013, 52, 8665−8676

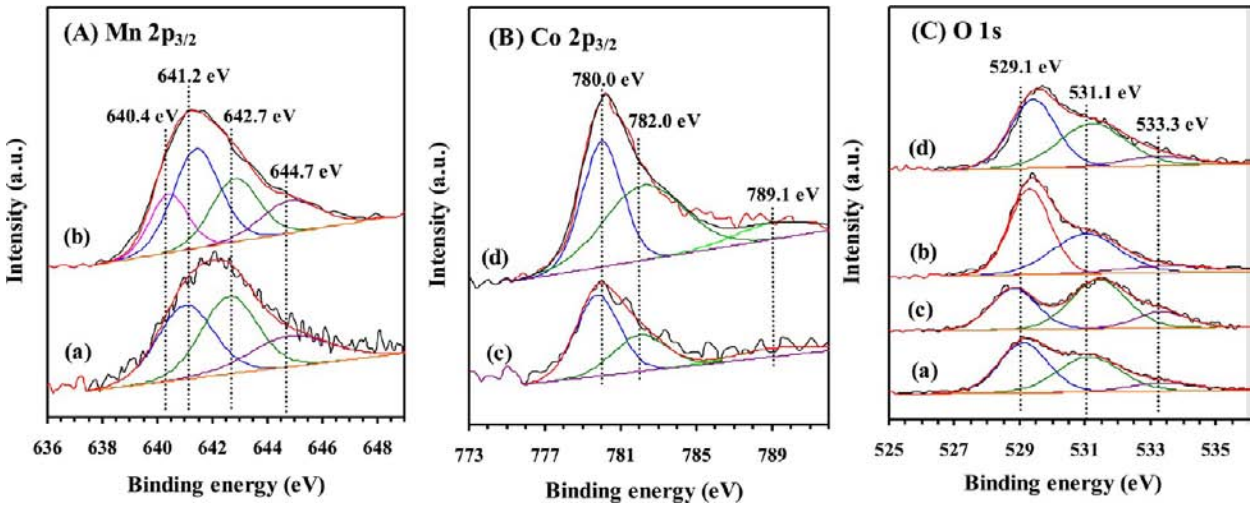

Figure 9. (A) Mn $2p_{3/2}$, (B) Co $2p_{3/2}$, and (C) O 1s XPS spectra of (a) hollow spherical $LaMnO_3$, (b) solid spherical Mn_2O_3, (c) hollow spherical $LaCoO_3$, and (d) solid spherical Co_3O_4.

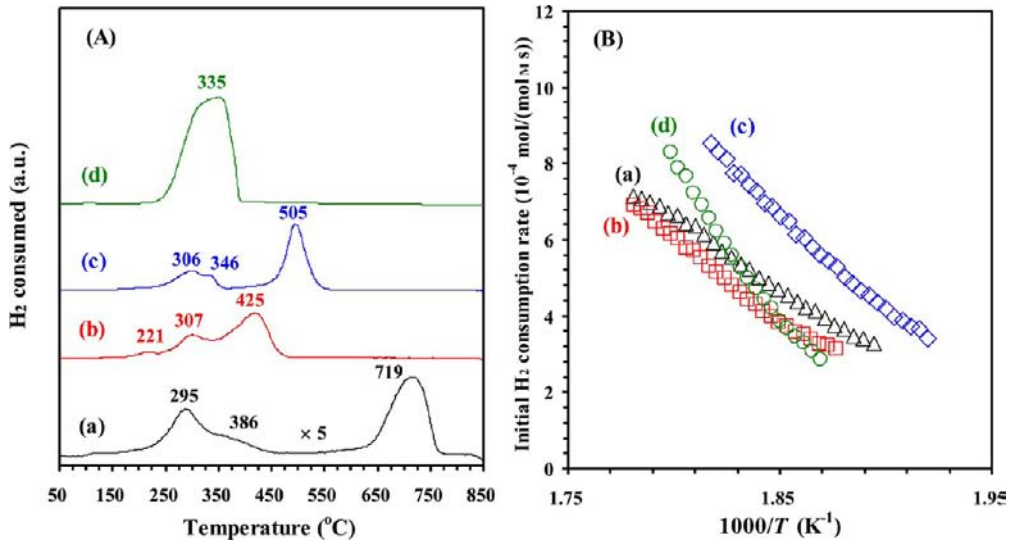

Figure 10. (A) H_2-TPR profiles and (B) initial H_2 consumption rate versus reverse temperature of (a) hollow spherical $LaMnO_3$, (b) solid spherical Mn_2O_3, (c) hollow spherical $LaCoO_3$, and (d) solid spherical Co_3O_4.

Effect of Metal Concentration and PEG Amount. The metal salt concentration and PEG amount are key factors in formation of hollow and solid spherical $LaMnO_3$ and Mn_2O_3 NPs. Figure 8 shows the SEM and TEM images of the $LaMnO_3$ samples obtained at different metal concentrations and PEG amounts. At metal concentration = 0.5 mol/L, irregularly morphological $LaMnO_3$ NPs (Figure 8a) were obtained; when the metal concentration rose to 2.5 mol/L, there was formation of uniform spherical $LaMnO_3$ NPs with a diameter of ca. 115 nm and connected skeletons (Figure 8b and 8c). In the absence of PEG, however, only 3DOM-structured $LaMnO_3$ material (Figure 8d) was obtained. With addition of 3 or 8 mL of PEG, uniform spherical $LaMnO_3$ NPs (Figure 8e and 8f) were generated. Obviously, appropriate metal concentration and PEG amount are beneficial for fabrication of monodispersed hollow spherical $LaMnO_3$ NPs.

Surface Composition, Metal Oxidation State, and Oxygen Species. XPS is an effective technique to gain the information related to the surface element compositions, metal oxidation states, and adsorbed species of a solid material. Figure 9 shows the Mn $2p_{3/2}$, Co $2p_{3/2}$, and O 1s spectra of the spherical $LaMO_3$ and MO_x samples. The asymmetrical XPS peaks can be decomposed by the curve-fitting approach. In the past years, a number of works on XPS characterization of manganese oxides have adopted the Mn $2p_{3/2}$ spectra for analysis of surface Mn^{4+}, Mn^{3+}, and Mn^{2+} species.[28,53−57] For the $LaMnO_3$ samples, there was the coexistence of Mn^{3+} and Mn^{4+} species.[43,58−60] As shown in Figure 9A, there was one asymmetrical signal at BE = ca. 642.0 eV for the hollow spherical $LaMnO_3$ sample and at BE = ca. 641.5 eV for the solid spherical Mn_2O_3 sample. The former could be decomposed into three components at BE = ca. 641.2, 642.7, and 644.7 eV, whereas the latter could be decomposed to four components at BE = 640.4, 641.5, 642.7, and 644.7 eV. The components at BE = ca. 640.4, 641.2−641.5, 642.7, and 644.7 eV were attributable to the surface Mn^{2+}, Mn^{3+}, and Mn^{4+} species and the satellite to the surface Mn^{3+} species,[43,61] respectively. From Figure 9B one Co $2p_{3/2}$ asymmetrical signal at BE = ca. 780.1 eV and a weak satellite peak at BE = ca. 789.1 eV due to the surface Co^{2+} species can be observed.[62] The former asymmetric signal could

dx.doi.org/10.1021/ic400832h | Inorg. Chem. 2013, 52, 8665−8676

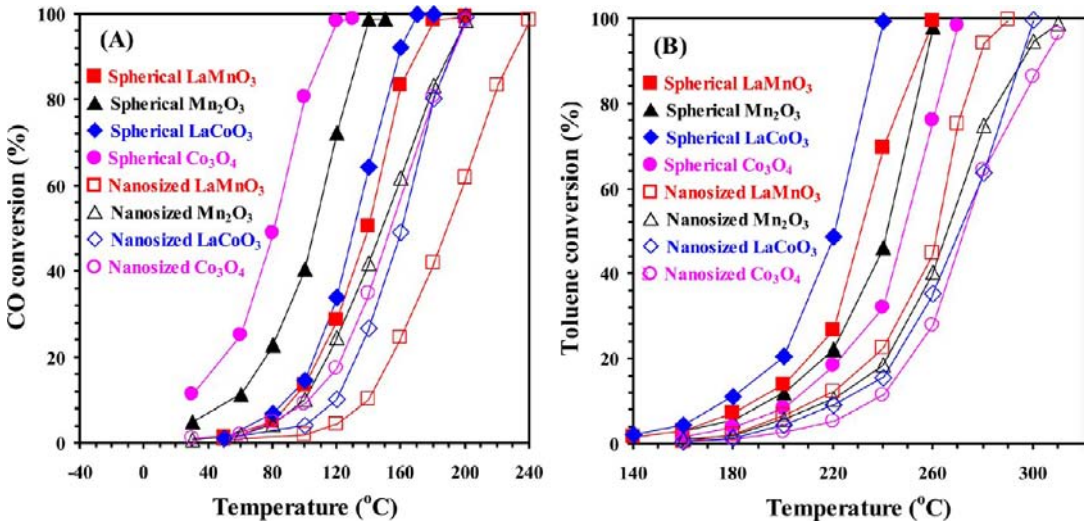

Figure 11. Catalytic activity as a function of reaction temperature over the spherical and nanosized $LaMO_3$ and MO_x samples under the conditions of (A) CO concentration = 1%, CO/O_2 molar ratio = 1/20, and SV = 10 000 mL/(g h) and (B) toluene concentration = 1000 ppm, toluene/O_2 molar ratio = 1/400, and SV = 20 000 mL/(g h).

be decomposed into two components at BE = ca. 780.0 and 782.0 eV assignable to the surface Co^{3+} and Co^{2+} species,[62] respectively. As can be seen from Figure 9C, the asymmetrical O 1s signal could be decomposed to three components at BE = ca. 529.1, 531.1, and 533.3 eV, attributable to the surface lattice oxygen (O_{latt}), adsorbed oxygen (O_{ads}, e.g., O_2^-, O_2^{2-}, O^-, OH^-, or CO_3^{2-}), and adsorbed molecular water,[60,63] respectively. Quantitative analyses on the Mn $2p_{3/2}$, Co $2p_{3/2}$, and O 1s XPS spectra of the samples give rise to the surface element compositions and Mn^{4+}/Mn^{3+} (or Mn^{3+}/Mn^{2+}), Co^{3+}/Co^{2+}, and O_{ads}/O_{latt} molar ratios, as summarized in Table 2. Surface Mn^{4+}/Mn^{3+} molar ratio in the hollow spherical $LaMnO_3$ sample, surface Mn^{3+}/Mn^{2+} molar ratio in the solid spherical Mn_2O_3 sample, and surface Co^{3+}/Co^{2+} molar ratios in the spherical $LaCoO_3$ and Co_3O_4 samples were 1.05, 2.09, 1.82, and 0.83, respectively. The surface O_{ads}/O_{latt} molar ratios were higher in the hollow spherical $LaMnO_3$ and $LaCoO_3$ samples than in the solid spherical Mn_2O_3 and Co_3O_4 samples, that is, the hollow spherical $LaMO_3$ samples possessed higher O_{ads} concentrations than the corresponding solid spherical MO_x samples. Figure S4, Supporting Information, shows Mn $2p_{3/2}$, Co $2p_{3/2}$, and O 1s spectra of the nanosized $LaMO_3$ and MO_x samples with a surface area of 4.5−9.6 m^2/g and a particle size of 100−300 nm (Figure S3, Supporting Information), and their surface element compositions are given in Table S1, Supporting Information. It is observed that the surface O_{ads}/O_{latt} and Mn^{4+}/Mn^{3+} (or Mn^{3+}/Mn^{2+}) and Co^{3+}/Co^{2+} molar ratios of the nanosized $LaMO_3$ samples were higher than those of the nanosized MO_x samples.

Reducibility. H_2-TPR is an ideal tool to examine the reducibility of a solid oxide sample. Figure 10A illustrates the H_2-TPR profiles of the spherical $LaMO_3$ and MO_x samples. Reduction of the hollow spherical $LaMnO_3$ sample took place in two steps: the reduction peaks at 200−450 °C was due to reduction of Mn^{4+} to Mn^{3+} as well as removal of oxygen adspecies, whereas the reduction peak at 719 °C was due to reduction of the remaining Mn^{3+} to Mn^{2+}.[64] In the case of the spherical Mn_2O_3 sample, there were reduction peaks at 221, 307, and 425 °C (Figure 10A(b)), corresponding to a total H_2 consumption of 7.46 mmol/g (Table S2, Supporting Information). According to the results reported previously,[23,65] the reduction process of manganese oxide could be reasonably divided into two steps: (i) $Mn^{4+} \rightarrow Mn^{3+}$ and (ii) $Mn^{3+} \rightarrow Mn^{2+}$. Theoretically, H_2 consumption for reduction of Mn_2O_3 to MnO is 6.30 mmol/g. In the present study, the total H_2 consumption (7.46 mmol/g) of the solid spherical Mn_2O_3 sample was higher than its theoretical H_2 consumption. This result indicates that there was the presence of Mn^{4+} and Mn^{3+} in the solid spherical Mn_2O_3 sample. The reduction peaks for the hollow spherical $LaCoO_3$ sample appeared at 306, 346, and 505 °C (Figure 10A(c)). Reduction of Co_3O_4 usually proceeds via the sequence of $Co_3O_4 \rightarrow CoO \rightarrow Co^0$.[66] The first two peaks at 306 and 346 °C were due to the reduction of Co^{3+} to Co^{2+} as well as the removal of the adsorbed oxygen species, whereas the reduction peak at 505 °C corresponded to reduction of Co^{2+} to Co^0.[67] It can be clearly seen from Figure 10A(d) that there was only one reduction peak at 335 °C, which was due to reduction of Co_3O_4 to Co^0. If the cobalt ions in cobalt oxide were only Co^{3+} and only Co^{2+} and reduced to Co^0, H_2 consumption would be 18.07 and 13.33 mmol/g, respectively. As revealed in our H_2-TPR result, H_2 consumption of the solid spherical Co_3O_4 sample was 15.48 mmol/g (Table S2, Supporting Information). Obviously, the cobalt ions in our cobalt oxide sample existed in a mixed valence (Co^{3+} and Co^{2+}), which was in good agreement with the result of XPS investigation. Figure S5A, Supporting Information, illustrates the H_2-TPR profiles of the nanosized $LaMO_3$ and MO_x samples. Apparently, the reduction temperatures of the nanosized samples were higher than those of the spherical counterparts, indicating that formation of small-sized metal oxide particles facilitated their reduction.

It has been generally accepted that the low-temperature reducibility of a sample can be conveniently evaluated using the initial (where less than 25% oxygen in the sample was removed for the first reduction peak) H_2 consumption rate.[68] Figures 10B and S5B (Supporting Information) show the initial H_2 consumption rate as a function of inverse temperature of the spherical and nanosized $LaMO_3$ and MO_x samples, respectively. It is clearly seen that the initial H_2 consumption rates of the samples decreased in the order of hollow spherical $LaCoO_3$ > hollow spherical $LaMnO_3$ ≈ solid spherical Mn_2O_3 ≈ solid spherical Co_3O_4 and of nanosized Co_3O_4 > nanosized $LaMnO_3$

dx.doi.org/10.1021/ic400832h | Inorg. Chem. 2013, 52, 8665−8676

Table 3. Catalytic Activities and Specific Reaction Rates of the Spherical and Nanosized $LaMO_3$ and MO_x (M = Mn and Co) Samples for CO and Toluene Oxidation, respectively

	CO or toluene oxidation activity[a] $T_{50\%}$ (°C)		CO or toluene oxidation activity[a] $T_{90\%}$ (°C)		Specific reaction rate[a] (μmol/(g s))	
catalyst	spherical	nanosized	spherical	nanosized	spherical	nanosized
$LaMnO_3$	141/231	202/267	169/254	231/278	0.155/0.032	0.0164/0.015
Mn_2O_3	106/242	148/266	132/258	189/296	0.080/0.027	0.014/0.013
$LaCoO_3$	131/220	161/271	157/237	190/295	0.180/0.047	0.0485/0.010
Co_3O_4	81/249	153/272	109/266	191/304	0.170/0.019	0.015/0.006

[a]Data before the "/" symbol are the $T_{50\%}$, $T_{90\%}$, or specific reaction rate of MO_x at 40 °C and $LaMO_3$ at 100 °C for CO oxidation, whereas data after the "/" symbol are the $T_{50\%}$, $T_{90\%}$, or specific reaction rate for toluene oxidation at 200 °C.

≈ nanosized $LaCoO_3$ > nanosized Mn_2O_3. Such change trends in low-temperature reducibility were in rough agreement with the sequences of their O_{ads} species concentrations and catalytic performance shown below.

Catalytic Performance. In the blank experiments (only quartz sands were loaded in the microreactor) under the conditions of CO concentration 1%, CO/O_2 molar ratio = 1/20, and SV = 10 000 mL/(g h) or (ii) toluene concentration = 1000 ppm, toluene/O_2 molar ratio = 1/400, and SV = 20 000 mL/(g h), no significant reactant conversions were observed at 250 °C for CO oxidation and at 400 °C for toluene combustion. These results indicate that no significant homogeneous reactions took place under the adopted reaction conditions. Figure 11 shows the catalytic activities of the as-fabricated samples. It is observed that CO or toluene conversion increased monotonously with the increase in reaction temperature. In order to better evaluate the activities of these samples, the temperatures ($T_{50\%}$ and $T_{90\%}$, respectively) required for 50% and 90% CO or toluene conversions are employed, as summarized in Table 3.

From Figure 12 it can be seen that the spherical $LaMO_3$ and MO_x samples outperformed the nanosized counterparts. For CO oxidation, the hollow spherical $LaCoO_3$ sample ($T_{50\%}$ = 131 °C and $T_{90\%}$ = 157 °C) showed better catalytic activity than the hollow spherical $LaMnO_3$ sample ($T_{50\%}$ = 141 °C and $T_{90\%}$ = 169 °C), whereas the solid spherical Co_3O_4 sample ($T_{50\%}$ = 81 °C and $T_{90\%}$ = 109 °C) was superior in performance to the solid spherical Mn_2O_3 sample ($T_{50\%}$ = 106 °C and $T_{90\%}$ = 132 °C). For toluene combustion, the hollow spherical $LaCoO_3$ sample ($T_{50\%}$ = 220 °C and $T_{90\%}$ = 237 °C) showed better catalytic activity than the hollow spherical $LaMnO_3$ sample ($T_{50\%}$ = 231 °C and $T_{90\%}$ = 254 °C) whereas the solid spherical Co_3O_4 sample ($T_{50\%}$ = 249 °C and $T_{90\%}$ = 266 °C) was inferior in performance to the solid spherical Mn_2O_3 sample ($T_{50\%}$ = 242 °C and $T_{90\%}$ = 258 °C).

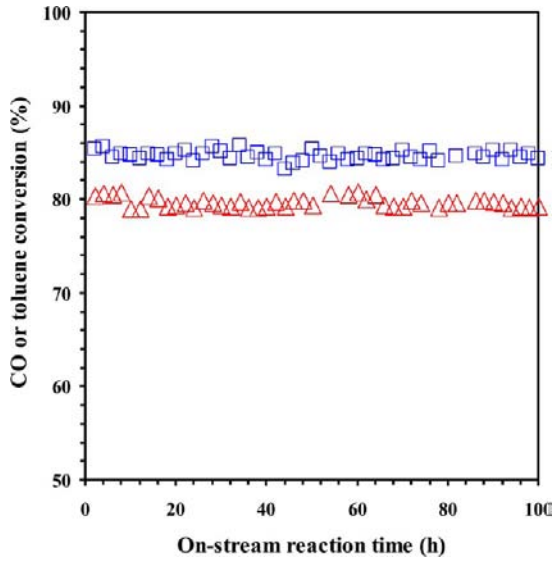

Figure 12. Catalytic activity versus on-stream reaction time over (△) solid spherical Co_3O_4 for CO oxidation under the conditions of CO concentration = 1%, CO/O_2 molar ratio = 1/20, SV = 10 000 mL/(g h), and temperature = 100 °C and (□) hollow spherical $LaCoO_3$ for toluene oxidation under the conditions of toluene concentration = 1000 ppm, toluene/O_2 molar ratio = 1/400, SV = 20 000 mL/(g h), and temperature = 230 °C.

It is better to compare the catalytic activities of the samples using their specific reaction rates, as shown in Figure S7, Supporting Information. The specific reaction rates of $LaMO_3$ at 100 °C and MO_x at 40 °C for CO oxidation and at 200 °C for toluene oxidation are summarized in Table 3. In the case of CO oxidation at 40 or 100 °C, the specific reaction rates of the spherical $LaMO_3$ and MO_x samples were much higher than those of the nanosized samples. The specific CO reaction rate at 100 °C of the hollow spherical $LaMnO_3$ sample was 0.155 μmol/(g s), higher than that (0.0344−0.0682 μmol/(g s)) achieved over the $LaMnO_3$ NPs reported in the literature.[69,70] The specific CO reaction rate at 40 °C (0.080 μmol/(g s)) of the solid spherical Mn_2O_3 sample was similar to that (0.065 μmol/(g s)) over the bulk Mn_2O_3 sample and that (0.101 μmol/(g s)) over the mesoporous Mn_2O_3 sample reported by other researchers.[27] In the case of toluene oxidation at 200 °C, the specific reaction rates of the spherical $LaMO_3$ and MO_x samples were much higher than those of the nanosized samples, with the highest specific reaction rate (0.047 μmol/(g s)) being achieved over the spherical $LaCoO_3$ sample. As shown in Table 3, the specific reaction rates at 200 °C of the hollow spherical $LaMnO_3$ and $LaCoO_3$ NPs were 0.032 and 0.047 μmol/(g s), respectively, much higher than that (0.015 μmol/(g s)) of nanosized $LaMnO_3$ and that (0.010 μmol/(g s)) of nanosized $LaCoO_3$ prepared in the present study and much higher than that (0.00038 μmol/(g s)) of the $LaMnO_3$ NPs reported in the literature.[30] The solid spherical Mn_2O_3 NPs gave a specific reaction rate at 200 °C of 0.027 μmol/(g s), much higher than that (0.0018 μmol/(g s)) of commercial Mn_3O_4[55] but lower than that (0.060 μmol/(g s)) of the flower-like Mn_2O_3 sample.[28] As for the solid spherical Co_3O_4, its specific rate at 200 °C (0.019 μmol/(g s)) was much higher than that (0.006 μmol/(g s)) of nanosized Co_3O_4 but lower than that (0.201 μmol/(g s)) of the mesoporous Co_3O_4 sample.[23]

Figure S8, Supporting Information, shows the effect of SV on the catalytic performance of the solid spherical Co_3O_4 and hollow spherical $LaCoO_3$ samples. As expected, CO or toluene

dx.doi.org/10.1021/ic400832h | Inorg. Chem. 2013, 52, 8665−8676

conversion increased with the drop in SV, indicating that the extension in contact time was favorable for conversion of CO or toluene. To examine the catalytic stability of the spherical $LaMO_3$ and MO_x samples, we carried out the 100 h on-stream reaction experiments; the results are shown in Figure 12. It is observed that there were no significant drops in catalytic activity within 100 h of on-stream reaction. Furthermore, the surface Co^{3+}/Co^{2+} and O_{ads}/O_{latt} molar ratios of the used sample after 100 h of CO or toluene oxidation (Table 2 and Figure S5, Supporting Information) were rather close to those of the fresh sample. Hence, we believe that the solid spherical Co_3O_4 and hollow spherical $LaCoO_3$ samples were catalytically durable.

Generally speaking, CO oxidation on transition metal oxides, such as MnO_x, CeO_2, Co_3O_4, and Fe_2O_3, follows a Mars–van Krevelen mechanism,[71] implying that lattice oxygen incorporation occurs during CO oxidation and the reduced surface of the metal oxide is replenished by gas-phase oxygen molecules.[72] Intensive studies on low-temperature CO oxidation over the Co_3O_4 and Mn_2O_3 catalysts have been performed by Yu et al.[73] and Xu et al.,[74] and it has been proposed that CO adsorption and reaction at low temperatures take place on the surface Co^{3+} and Mn^{3+} sites, respectively. Therefore, the higher CO reactivity over Co_3O_4 and Mn_2O_3 than over $LaCoO_3$ and $LaMnO_3$ might be attributed to the abundant surface-exposed metal ions, which could give a stronger adsorption. The catalytic activity over Co_3O_4 for CO oxidation is superior to that over Mn_2O_3, which is associated with the lower metal–oxygen bond energy of Co_3O_4.[75] It has been generally accepted that the performance of an ABO_3 catalyst is related to its defect nature and density, oxygen adspecies, and reducibility. The presence of oxygen nonstoichiometry favors activation of gas-phase oxygen molecules to form active oxygen adspecies. The higher the oxygen nonstoichiometry, the better the performance of the perovskite catalyst.[19] Since toluene is rather stable, its oxidation mechanism might be as follows. Toluene is mainly oxidized by the surface-adsorbed oxygen species at low temperatures, and the surface-adsorbed oxygen species could attack an organic molecule where the electron density is the highest;[76] thus, total oxidation of VOCs would take place more readily. By comparing the XPS data of the as-obtained catalysts, it can be noticed that the perovskite-type oxides contained larger amounts of adsorbed oxygen species than the metal oxides. Hence, $LaMnO_3$ and $LaCoO_3$ exhibited better catalytic activities than Co_3O_4 and Mn_2O_3 for toluene oxidation. The spherical catalysts derived from the PMMA-templating route showed much higher catalytic activities than the conventional nanosized catalysts. On one hand, a high surface area indicates that larger amounts of active sites were exposed and even larger amounts of structural defects were formed on the surface of the materials. On the other hand, compared to the nanosized catalysts, the first reduction step of the spherical catalysts shifted to a lower temperature, suggesting that a higher reactivity of lattice oxygen at low temperatures would give rise to an easier redox process of $M^{(n+1)+}$ to M^{n+} (M = Mn and Co). The increase in mobility of lattice oxygen in our catalysts could be beneficial for the enhancement in catalytic performance of the materials.

CONCLUSIONS

The uniform hollow spherical perovskite-type oxides $LaMO_3$ and solid spherical transition-metal oxides MO_x (M = Mn and Co) NPs could be synthesized using the PMMA-templating method. The hollow spherical $LaMO_3$ and solid spherical MO_x NPs possessed rhombohedral and cubic crystal structures with surface areas of 21–33 and 21–24 m^2/g, respectively. There was a larger amount of surface O_{ads} species on $LaMO_3$ than on MO_x. The hollow spherical $LaMO_3$ samples also possessed better low-temperature reducibility than the solid spherical MO_x samples. The spherical $LaMO_3$ and MO_x samples outperformed the nanosized counterparts for oxidation of CO and toluene. For CO oxidation at SV = 10 000 mL/(g h), the hollow spherical $LaCoO_3$ ($T_{50\%}$ = 131 °C and $T_{90\%}$ = 157 °C) and solid spherical Co_3O_4 ($T_{50\%}$ = 81 °C and $T_{90\%}$ = 109 °C) samples showed better catalytic activity than the hollow spherical $LaMnO_3$ ($T_{50\%}$ = 141 °C and $T_{90\%}$ = 169 °C) and solid spherical Mn_2O_3 ($T_{50\%}$ = 106 °C and $T_{90\%}$ = 132 °C) samples, respectively. For toluene oxidation at SV = 20 000 mL/(g h), the hollow spherical $LaCoO_3$ ($T_{50\%}$ = 220 °C and $T_{90\%}$ = 237 °C) and solid spherical Mn_2O_3 ($T_{50\%}$ = 242 °C and $T_{90\%}$ = 258 °C) samples outperformed the hollow spherical $LaMnO_3$ sample ($T_{50\%}$ = 231 °C and $T_{90\%}$ = 254 °C) and solid spherical Co_3O_4 sample ($T_{50\%}$ = 249 °C and $T_{90\%}$ = 266 °C), respectively. It is concluded that the excellent catalytic performance of the hollow spherical $LaCoO_3$ and solid spherical Co_3O_4 NPs is associated with their higher surface areas and O_{ads} concentrations and better low-temperature reducibility. We are sure that the PMMA-templating strategy can provide an effective pathway to generate uniform spherical perovskite-type oxide and transition-metal oxide NPs.

ASSOCIATED CONTENT

Supporting Information

Additional preparation conditions, nitrogen adsorption–desorption isotherms, SEM images of the nanosized samples and well-aligned PMMA microspheres, H_2-TPR profiles of the nanosized samples, CO or toluene consumption rates over the samples, and effect of SV on the catalytic activity of the samples. This material is available free of charge via the Internet at http://pubs.acs.org.

AUTHOR INFORMATION

Corresponding Author

*Phone: +8610-6739-6118. Fax: +8610-6739-1983. E-mail: hxdai@bjut.edu.cn.

Notes

The authors declare no competing financial interest.

ACKNOWLEDGMENTS

The work described above is financially supported by the NSF of China (20973017 and 21077007), the Discipline and Postgraduate Education (005000541212014 and 005000542513001), and the Funding Project for Academic Human Resources Development in Institutions of Higher Learning under the Jurisdiction of Beijing Municipality (PHR201207104). We also thank Prof. Chak Tong Au (Department of Chemistry, Hong Kong Baptist University) and Mrs. Jianping He (State Key Laboratory of Advanced Metals and Materials, University of Science & Technology Beijing) for doing the XPS and SEM analyses, respectively.

REFERENCES

(1) Kim, S. W.; Kim, M.; Lee, W. Y.; Hyeon, T. *J. Am. Chem. Soc.* **2002**, *124*, 7642.

(2) Zhang, J.; Liu, X.; Wu, S.; Xu, M.; Guo, X.; Wang, S. *J. Mater. Chem.* **2010**, *20*, 6453.

(3) Hung, L. I.; Tsung, C. K.; Huang, W.; Yang, P. *Adv. Mater.* **2010**, *22*, 1910.
(4) Li, J.; Zeng, H. C. *Angew. Chem., Int. Ed.* **2005**, *44*, 4342.
(5) Cheng, K.; Peng, S.; Xu, C.; Sun, S. *J. Am. Chem. Soc.* **2009**, *131*, 10637.
(6) Lou, X. W.; Wang, Y.; Yuan, C.; Lee, J. Y.; Archer, L. A. *Adv. Mater.* **2006**, *18*, 2325.
(7) Li, J.; Zeng, H. C. *J. Am. Chem. Soc.* **2007**, *129*, 15839.
(8) Sun, X. M.; Liu, J. F.; Li, Y. D. *Chem.—Eur. J.* **2006**, *12*, 2039.
(9) Park, J. U.; Lee, H. J.; Cho, W.; Jo, C.; Oh, M. *Adv. Mater.* **2011**, *23*, 3161.
(10) Li, X.; Tang, C. J.; Ai, M.; Dong, L.; Xu, Z. *Chem. Mater.* **2010**, *22*, 4879.
(11) Tian, X. L.; Li, J.; Chen, K.; Han, J.; Pan, S. L.; Wang, Y. J.; Fan, X. Y.; Li, F.; Zhou, Z. X. *Cryst. Growth Des.* **2010**, *10*, 3990.
(12) Lu, Z. G.; Tang, Y. G.; Chen, L. M.; Li, Y. D. *J. Cryst. Growth* **2004**, *266*, 539.
(13) Gu, J. M.; Li, S. H.; Ju, M. L.; Wang, E. B. *J. Cryst. Growth* **2011**, *320*, 46.
(14) Kim, Y. N.; Kim, J. C.; Lee, E. K.; Hwang, Y. S.; Hur, N. H.; Yun, Y. J.; Park, G. S.; Kim, J. T. *J. Appl. Phys.* **2004**, *95*, 7088.
(15) Zhang, X. X.; Zhang, T.; Gu, F. B.; Wang, Z. H.; Guo, G. S. *Environ. Chem. (in Chinese)* **2011**, *30*, 808.
(16) Park, J.; Joo, J.; Kwon, S. G.; Jang, Y.; Hyeon, T. *Angew. Chem., Int. Ed.* **2007**, *46*, 4630.
(17) Li, F.; Qian, Y. Q.; Stein, A. *Chem. Mater.* **2010**, *22*, 3226.
(18) Li, F.; Delo, S. A.; Stein, A. *Angew. Chem., Int. Ed.* **2007**, *46*, 6666.
(19) Pena, M. A.; Fierro, J. L. G. *Chem. Rev.* **2001**, *101*, 1981.
(20) Hu, L. H.; Sun, K. Q.; Peng, Q.; Xu, B. Q.; Li, Y. D. *Nano Res.* **2010**, *3*, 363.
(21) Weidenkaff, A. *Adv. Eng. Mater.* **2004**, *6*, 709.
(22) Peluso, M. A.; Pronsato, E.; Sambeth, J. E.; Thomas, H. J.; Busca, G. *Appl. Catal., B* **2008**, *78*, 73.
(23) Deng, J. G.; Zhang, L.; Dai, H. X.; Xia, Y. S.; Jiang, H. Y.; Zhang, H.; He, H. *J. Phys. Chem. C* **2010**, *114*, 2694.
(24) Xie, X. W.; Li, Y.; Liu, Z. Q.; Haruta, M.; Shen, W. J. *Nature* **2009**, *458*, 746.
(25) Garcia, T.; Agouram, S.; Sánchez-Royo, J. F.; Murillo, R.; Mastral, A. M.; Aranda, A.; Vázquez, I.; Dejoz, A.; Solsona, B. *Appl. Catal., A* **2010**, *386*, 16.
(26) Tüysüz, H.; Comotti, M.; Schüth, F. *Chem. Commun.* **2008**, 4022.
(27) Ren, Y.; Ma, Z.; Qian, L. P.; Dai, S.; He, H. Y.; Bruce, P. G. *Catal. Lett.* **2009**, *131*, 146.
(28) Wang, F.; Dai, H. X.; Deng, J. G.; Bai, G. M.; Ji, K. M.; Liu, Y. X. *Environ. Sci. Technol.* **2012**, *46*, 4034.
(29) Xia, Y. S.; Dai, H. X.; Jiang, H. Y.; Zhang, L. *Catal. Commun.* **2010**, *11*, 1171.
(30) Irusta, S.; Pina, M. P.; Menéndez, M.; Santamaría, J. *J. Catal.* **1998**, *179*, 400.
(31) Spinicci, R.; Faticanti, M.; Marini, P.; De Rossi, S.; Porta, P. *J. Mol. Catal. A* **2003**, *197*, 147.
(32) Li, H. N.; Zhang, L.; Dai, H. X.; He, H. *Inorg. Chem.* **2009**, *48*, 4421.
(33) Ciambelli, P.; Cimino, S.; Rossi, S. D.; Faticanti, M.; Lisi, L.; Minelli, G.; Pettiti, I.; Porta, P.; Russo, G.; Turco, M. *Appl. Catal., B* **2000**, *24*, 243.
(34) Hechavarría, L.; Mendoza, N.; Altuzar, P.; Hu, H. *J. Solid State Electrochem.* **2010**, *14*, 323.
(35) Striker, T.; Ruud, J. A. *J. Am. Ceram. Soc.* **2010**, *93*, 2622.
(36) Yan, H. W.; Blanford, C. F.; Lytle, J. C.; Carter, C. B.; Smyrl, W. H.; Stein, A. *Chem. Mater.* **2001**, *13*, 4314.
(37) Zhou, W.; Ran, R.; Shao, Z. P.; Jin, W. Q.; Xu, N. P. *Bull. Mater. Sci.* **2010**, *33*, 371.
(38) Zhang, R. Z.; Dai, H. X.; Du, Y. C.; Zhang, L.; Deng, J. G.; Xia, Y. S.; Zhao, Z. X.; Meng, X.; Liu, Y. X. *Inorg. Chem.* **2011**, *50*, 2534.
(39) Shafi, K. V. P. M.; Ulman, A.; Yan, X.; Yang, N. L.; Estournès, C.; White, H.; Rafailovich, M. *Langmuir* **2001**, *17*, 5093.
(40) Wu, Y. T.; Wang, X. F. *Mater. Lett.* **2011**, *65*, 2062.
(41) Li, J. S.; Wei, X. T.; Lin, Y. S.; Su, D. *J. Membr. Sci.* **2008**, *312*, 186.
(42) Moussaif, N.; Irusta, S.; Yagüe, C.; Arruebo, M.; Meier, J. G.; Crespo, C.; Jimenez, M. A.; Santamaría, J. *Polymer* **2010**, *51*, 6132.
(43) Ponce, S.; Peña, M. A.; Fierro, J. L. G. *Appl. Catal., B* **2000**, *24*, 193.
(44) Bernard, C.; Durand, B.; Verelst, M.; Lecante, P. *J. Mater. Sci.* **2004**, *39*, 2821.
(45) Yin, Y. D.; Rioux, R. M.; Erdonmez, C. K.; Hughes, S.; Somorjai, G. A.; Alivisatos, A. P. *Science* **2004**, *30*, 711.
(46) Fan, H. J.; Knez, M.; Scholz, R.; Nielsch, K.; Pippel, E.; Hesse, D.; Zacharias, M.; Gösele, U. *Nat. Mater.* **2006**, *5*, 627.
(47) Chang, Y.; Teo, J. J.; Zeng, H. C. *Langmuir* **2005**, *21*, 1074.
(48) Sadakane, M.; Horiuchi, T.; Kato, N.; Takahashi, C.; Ueda, W. *Chem. Mater.* **2007**, *19*, 5779.
(49) Sadakane, M.; Takahashi, C.; Kato, N.; Ogihara, H.; Nodasaka, Y.; Doi, Y.; Hinatsu, Y.; Ueda, W. *Bull. Chem. Soc. Jpn.* **2007**, *80*, 677.
(50) Xu, J. F.; Liu, J.; Zhao, Z.; Xu, C. M.; Zheng, J. X.; Duan, A. J.; Jiang, G. Y. *J. Catal.* **2011**, *282*, 1.
(51) Tao, F. F.; Gao, C. L.; Wen, Z. H.; Wang, Q.; Li, J. H.; Xu, Z. *J. Solid State Chem.* **2009**, *182*, 1055.
(52) An, T. C.; Liu, J. K.; Li, G. Y.; Zhang, S. Q.; Zhao, H. J.; Zeng, X. Y.; Sheng, G. Y.; Fu, J. M. *Appl. Catal., A* **2008**, *350*, 237.
(53) Dai, Y.; Wang, X. Y.; Dai, Q. G.; Li, D. *Appl. Catal., B* **2012**, *111−112*, 141.
(54) Qu, Z. P.; Bu, Y. B.; Qin, Y.; Wang, Y.; Fu, Q. *Appl. Catal., B* **2013**, *132−133*, 353.
(55) Kim, S. C.; Shim, W. G. *Appl. Catal., B* **2010**, *98*, 180.
(56) Santos, V. P.; Pereira, M. F. R.; Orfao, J. J. M.; Figueiredo, J. L. *Top. Catal.* **2009**, *52*, 470.
(57) Delimaris, D.; Ioannides, T. *Appl. Catal., B* **2008**, *84*, 303.
(58) Töpfer, J.; Feltz, A.; Graf, D.; Hackl, B.; Raupach, L.; Weissbrodt, P. *Phys. Status Solidi* **1992**, *134*, 405.
(59) Najjar, H.; Batis, H. *Appl. Catal., A* **2010**, *383*, 192.
(60) Machocki, A.; Ioannides, T.; Stasinska, B.; Gac, W.; Avgouropoulos, G.; Delimaris, D.; Grzegorczyk, W.; Pasieczna, S. *J. Catal.* **2004**, *227*, 282.
(61) Tseng, T. K.; Chu, H.; Hsu, H. H. *Environ. Sci. Technol.* **2003**, *37*, 171.
(62) Fierro, G.; Jacono, Lo, M.; Inversi, M.; Dragone, R.; Porta, P. *Top. Catal.* **2000**, *10*, 39.
(63) Zhang, C. H.; Wang, C.; Zhan, W. C.; Guo, Y. L.; Guo, Y.; Lu, G. Z.; Baylet, A.; Giroir-Fendler, A. *Appl. Catal., B* **2013**, *129*, 509.
(64) Teng, F.; Han, W.; Liang, S. H.; Gaugeu, B.; Zong, R. L.; Zhu, Y. F. *J. Catal.* **2007**, *250*, 1.
(65) Stobbe, E. R.; de Boer, B. A.; Geus, J. W. *Catal. Today* **1999**, *47*, 161.
(66) Teng, F.; Chen, M. D.; Li, G. Q.; Teng, Y.; Xu, T. G.; Hang, Y. C.; Yao, W. Q.; Santhanagopalane, S.; Meng, D. D.; Zhu, Y. F. *Appl. Catal., B* **2011**, *110*, 133.
(67) Sextori, B. A.; Hughes, A. E.; Turney, T. W. *J. Catal.* **1986**, *97*, 390.
(68) Chen, K. D.; Xie, S. B.; Bell, A. T.; Iglesia, E. *J. Catal.* **2001**, *198*, 232.
(69) Cimino, S.; Colonna, S.; De Rossi, S.; Faticanti, M.; Lisi, L.; Pettiti, I.; Portaz, P. *J. Catal.* **2002**, *205*, 309.
(70) Abdolrahmani, M.; Parvari, M.; Habibpoor, M. *J. Catal.* **2010**, *31*, 394.
(71) Jansson, J. *J. Catal.* **2000**, *194*, 55.
(72) Xu, R.; Wang, X.; Wang, D. S.; Zhou, K. B.; Li, Y. D. *J. Catal.* **2006**, *237*, 426.
(73) Yu, Y. B.; Takei, T.; Ohashi, H.; He, H.; Zhang, X. L.; Haruta, M. *J. Catal.* **2009**, *267*, 121.
(74) Xu, J.; Deng, Y. Q.; Luo, Y.; Mao, W.; Yang, X. J.; Han, Y. F. *J. Catal.* **2013**, *300*, 225.
(75) Boreskov, G. K. *Kinet. Catal.* **1967**, *8*, 878.
(76) Bielañski, A.; Haber, J. *Oxygen in Catalysis*; Marcel Dekker: New York, 1991; pp 392.